AAS 24-355

# COVARIANCE PREDICTION VALIDATION AND PERTURBATION RECOVERY FOR A CREWED STATION IN A NEAR RECTILINEAR HALO ORBIT

Clark P. Newman,* Matt Gualdoni,† Diane C. Davis‡

The Gateway mission will place a crew-tended station in orbit near the Moon to support surface and heliocentric operations. The uncertainty of the Gateway state is captured in its covariance, which is used to calculate collision risk with visiting vehicles (VV). The predicted covariance is validated against Monte Carlo predictions of state dispersions to validate collision risk calculations. Additionally, the recovery of Gateway state and covariance following a docking/undocking event as a function of post-event tracking and post-tracking prediction are calculated. This analysis is to determine the time and tracking data required to recover from a docking perturbation.

## INTRODUCTION

The Gateway mission is built around the Gateway station which will be in an Earth-Moon Southern L2 Near Rectilinear Halo Orbit (NRHO).[1] The specific mission NRHO has a 9:2 lunar synodic resonance, which means that the vehicle will complete nine revolutions in the NRHO as the Moon completes two revolutions around the Earth. This trajectory is repeatable in the Earth-Sun rotating system, creating nine positions of perilune crossing that remain relatively constant in relation to Earth and Sun.[2]

From its trajectory in the NRHO, the Gateway station can support cislunar, lunar surface, and heliocentric operations. It has constant line-of-sight connection to Earth, avoids eclipses, and has multi-day views of the lunar south pole every revolution.[345] Visiting vehicles (VV) can join the Gateway on the NRHO and either approach to dock, or loiter in the vicinity of Gateway.[6]

Artemis IV is planned to stage at the Gateway—Orion and the Human Lander System (HLS) will both dock to Gateway, the crew will transfer to HLS, and HLS will depart for the lunar surface sortie. After one NRHO revolution the HLS will return to NRHO to dock with Gateway, the crew will transfer back to Orion, and they will depart to return to Earth.[7]

### Tracking and Filtering

The Gateway vehicle will be tracked by Earth stations, whose tracking data is processed Earth-side and state updates are delivered to the vehicle, used for Orbit Maintenance Maneuver (OMM) calculations, and distributed to partners for VV mission planning.[8] For these analyses, the Gateway is tracked by Deep Space Network (DSN) primary stations and European Space Agency's (ESA)

---

*Project Engineer, a.i. solutions, Inc.

†GN&C Engineer, NASA JSC

‡Gateway Mission Design Lead, NASA JSC

Estrack stations.[9] The Gateway is tracked with three eight-hour tracking passes per NRHO revolution while uncrewed. While crewed, it is tracked with three six-hour passes *per day*, which adds up to 18 hours of tracking every day.

The uncrewed tracking schedule is depicted on the NRHO in Figure 1. Starting at perilune, the first post-perilune tracking data pass is labeled B and is chosen within a 23 hour window starting one hour after perilune. The next pass, labeled E, is the pre-OMM tracking data pass and is chosen within a 24 hour window that ends 24 hours before OMM execution. Finally, the post-OMM (or pre-perilune if you prefer) tracking data pass is labeled A and is chosen from a 23 hour window that ends one hour prior to perilune.[10]

Nominally, the Gateway estimated state is calculated at the data cut off (DCO) of pass *E*, after processing the tracking data passes available.[11] The OMM is calculated with the estimated state by targeting the perilune state six NRHO revolutions ahead in a receding horizon targeting algorithm. The Earth-Moon rotating X-direction velocity and Y-direction position is targeted to match the reference trajectory.[12] The OMM is then executed at a true anomaly of $\nu = 200°$ and the cycle repeats for the next NRHO revolution. OMMs targeted with a magnitude below 3 cm/s are waived, which occurs frequently during uncrewed operations.[13]

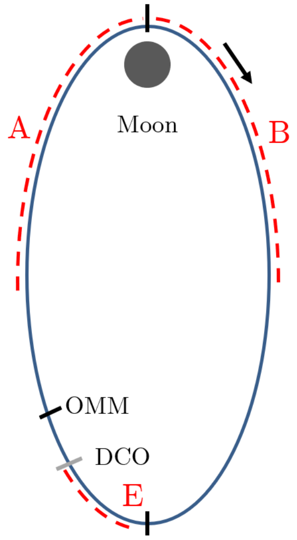

**Figure 1: Nominal tracking data arcs visualized on the NRHO for uncrewed operations.**

### HLS Mission Timelines

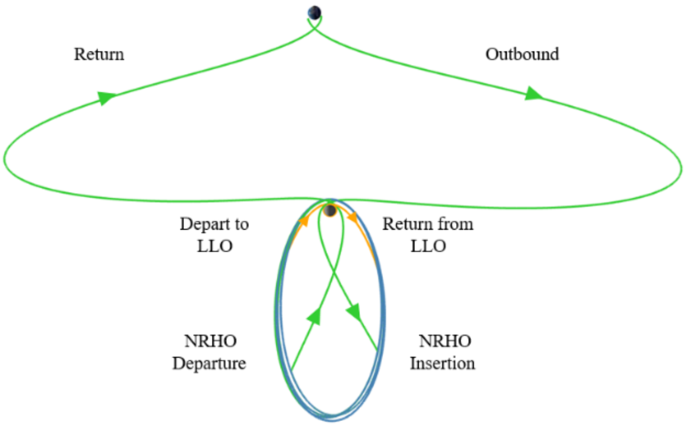

**Figure 2: Lunar mission concept: the NRHO in blue, surface excursions in orange, and direct transfers in green, as viewed in the Earth-Moon rotating frame.**

Figure 2 shows a depiction of trajectories involved in an HLS mission through Gateway. On the right, the Outbound trajectory is a direct transfer from Earth to the Moon. At the Moon, the vehicle (Orion or HLS in this case) will perform a Outbound Powered Flyby (OPF) to realign to the NRHO plane and establish the intercept with Gateway. When the vehicle reaches NRHO it will perform the NRHO Insertion (NRI) maneuver to rendezvous with the Gateway (labeled “NRHO Insertion”). To perform the lunar surface sortie, the HLS will undock and transfer to Low Lunar Orbit (LLO)(labeled “Depart to LLO”). The HLS will land in the southern hemisphere and conduct surface operations while Gateway traverses one revolution of the NRHO. The HLS will then launch (labeled “Return to NRHO”) and rendezvous with Gateway. Finally, Orion will undock (labeled “NRHO Departure”) and perform the NRHO Departure burn (NRD) followed by the Return Powered Flyby (RPF) to traverse the return leg (labeled "Return") back to Earth.

During an HLS mission timeline, the OMM execution true anomaly can be shifted to $\nu = 180°$ to deconflict the OMM execution with HLS mission timeline activities like RPOD events. The presence of Orion and/or HLS induces velocity perturbations to the Gateway state through attitude maneuvers, reaction wheel assembly (RWA) desaturation maneuvers, $CO_2$ venting, wastewater venting, and HLS venting.

As mentioned earlier, the crewed Gateway is tracked at a high cadence of three eight hour passes per day. The high cadence is to maintain acceptable state errors while subject to increased velocity perturbations. Under this operations regime, the DCO for OMM targeting is 24 hours prior to execution, be it at $\nu = 200°$ or elsewhere on the NRHO.

## Covariance Propagation

The navigation algorithm utilizes a Square Root Information Filter (SRIF) which produces a state estimate and covariance. The covariance describes the state uncertainty and correlations as Gaussian distributions, and can be visualized as an ellipsoidal cloud of uncertainty like in Figure 3. Starting at the bottom left, the post-DCO state estimate $\hat{\boldsymbol{x}}(t_0)$ and covariance $\mathrm{P}(t_0)$ are propagated through time $t_n$ to the final time $t_f$. Generally (though not always) velocity uncertainty integrates into position uncertainty which causes the covariance to "grow" over time, as is shown in Figure 3. The truth state $\boldsymbol{x}(t)$ is deviated by the estimation error, ideally this deviation's behavior over time is captured by the propagation of the covariance. A Monte Carlo analysis of distribution of true state errors should return a distribution that is well-described by the propagated covariance.[14]

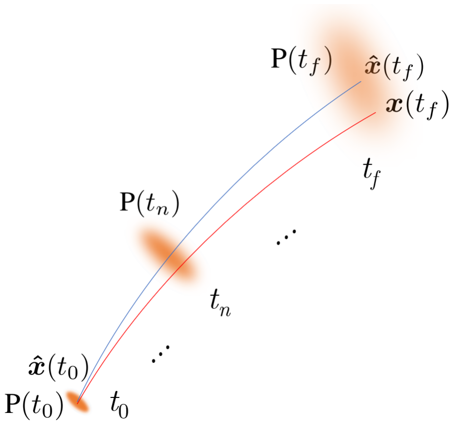

**Figure 3: State estimate $\hat{\boldsymbol{x}}(t)$ and covariance $\mathbf{P}(t)$ propagated through time from $t_0$ to $t_f$**

The covariance propagation relies on linearization about the estimated state to map the STM forward in time. The covariance is propagated in a nonlinear force model with

$$\dot{\mathbf{P}}(t) = \mathbf{F}(t)\mathbf{P}(t) + \mathbf{P}(t)\mathbf{F}(t)^T + \mathbf{Q}(t), \tag{1}$$

where

$$\mathbf{F}(t) = \left.\frac{\delta f}{\delta \mathbf{x}}\right|_{\hat{\mathbf{x}}(t),\mathbf{u}(t)}, \tag{2}$$

and $\mathbf{Q}(t)$ is the spectral density matrix of the state process noise. The covariance is integrated forward in time about a linear approximation of the force model evaluated at the estimated state. Filter process noise can compensate for force model linearization and unmodeled perturbations, at the cost of inflating the covariance larger than the distribution of state errors. This is useful to ensure a navigation filter that is robust against diverging but can result in conservative state estimation uncertainties that do not accurately capture the distribution of state estimation uncertainty. A covariance that closely models the state estimate uncertainty is important for mission planning, particularly for collision avoidance calculations. A conservative covariance can “dilute” the state estimate which results in untrustworthy calculations of collision probability.

## SIMULATION PARAMETERS

### MiDAS

The navigation simulation is executed in the Determining Orbit of Gateway (DOG) component of Mission Design and Analysis Software (MiDAS), a simulation suite developed at NASA Johnson Space Center for Gateway Mission Design. MiDAS combines three components to produce a high fidelity simulation that includes attitude control, contact analysis, and orbit determination (OD) analysis. A simplified flow chart of MiDAS automation is depicted in Figure 4.

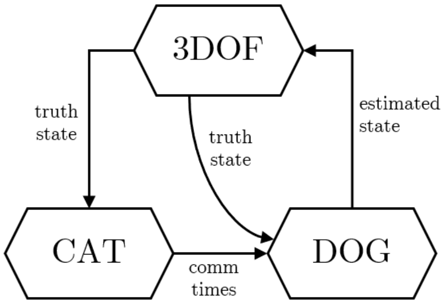

**Figure 4: MiDAS functional flow chart.**

Starting at the top, the high fidelity mission simulator 3DOF models the truth trajectory from a post-OMM state and considers a flat plate model for Gateway, integrates angular momentum, selects thrusters for maneuvers, and targets the OMM. It produces a truth ephemeris and attitude history which is fed to the Comm Analysis Tool (CAT), which considers Gateway 3D models, antenna locations and gimbal range, and produces a time history of valid communication windows with Earth ground sites. This schedule and the truth ephemeris are input to DOG which simulates tracking data per the mission tracking schedule and received valid communications times from CAT. It then processes the tracking data in a SRIF to produce a state estimate at the final DCO. This estimated state is input back into 3DOF to target the next revolution’s OMM. The OMM is executed (with random execution errors) on the truth state, and the cycle repeats for another NRHO revolution.

Below in Tables 1 and 2, error sources and data parameters are listed, respectively. Tracking data is assumed to be X-band range and range rate with an observation rate of one per minute.

**Table 1: Simulated Error Sources**

| Parameter Name | 1-$\sigma$ uncertainty |
|---:|:---:|
| Initial Position Error | 10 km |
| Initial Velocity Error | 10 cm/s |
| Relative Mass Error | 30% |
| Relative SRP Area Error | 30% |
| Desaturation Maneuver $\Delta$V | 3.33 mm/s |
| Uncrewed OMM Constant Error | 0.47 mm/s |
| Uncrewed OMM Magnitude Error | 0.5% |
| Crewed OMM Magnitude Error | 0.5% |
| OMM Pointing Error | 0.333° |

**Table 2: Tracking Data Quality Parameters**

| Parameter | Value (1-$\sigma$) |
|---:|:---:|
| Range Noise (m) | 1.0 |
| Range Bias (m) | 7.5 |
| Range-Rate Noise (mm/s) | 0.2 |

## COVARIANCE VALIDATION

As mentioned previously, the ability for a propagated covariance to accurately model the state estimate error dispersion is important for accurate calculations of stochastic events, such as the probability of collision with a secondary object. Filter process noise is increased to compensate for errors from unmodeled perturbations, unobservable range bias, and linearity assumptions. These efforts will make the filter robust against divergence but can produce a state estimate covariance that is more conservative than true state errors.

To validate the accuracy of propagated filter covariances, a Monte Carlo analysis is performed to produce a set of state estimation error dispersions to compare against filter covariances. For a particular epoch, the filter state estimate and covariance are saved across every Monte Carlo iteration. From that epoch, each state estimate is propagated forward in time while comparing the state error distribution across Monte Carl iterations to the propagated filter covariance. Due to the dynamic geometry of the NRHO, the analysis is repeated at multiple epochs for total coverage of the NRHO.

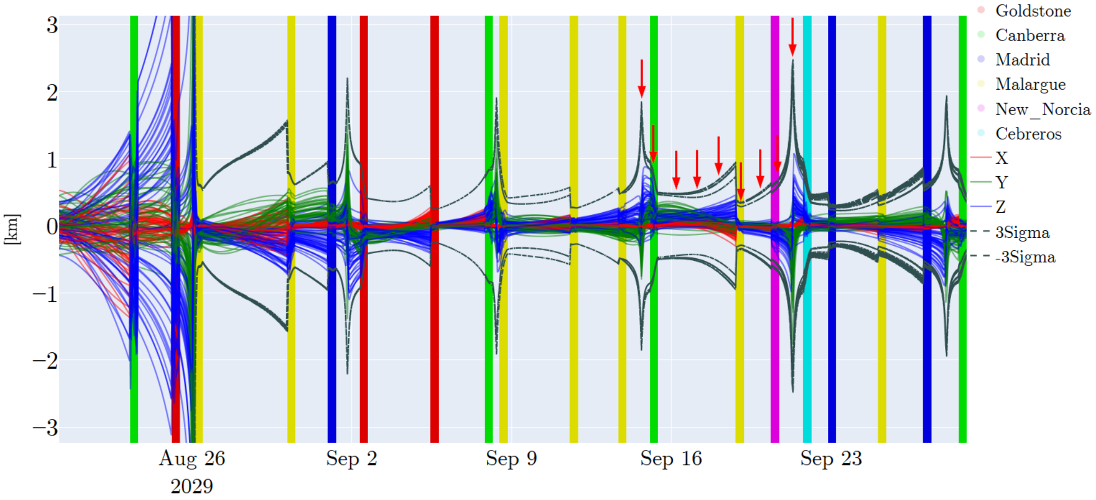

**Figure 5: Earth-Moon rotating position errors and filter sigma over six uncrewed NRHO revolutions. Vectors are saved for prediction during the revolution marked with red arrows.**

The sampled predictive estimation errors are compared to the propagated filter covariances for predictions starting at various points around the NRHO to capture the dynamics of the entire orbit. The simulation is initialized and run for four revolutions to achieve steady-state behavior, and on the fourth NRHO revolution vectors from around the orbit are saved for predictions. The position error and uncertainty over time for the definitive span of this simulation is shown in Figure 5. The red, green, and blue lines track the position error in Earth Moon rotating frame X, Y, and Z-directions, respectively. The dashed gray line represents the filter 3-$\sigma$ uncertainty, and the highlighted timespans correspond to periods of ground tracking by specific ground sites. The initial errors and uncertainty on the left collapse to steady-state behavior after two NRHO revolutions. NRHO revolutions are punctuated by perilune passages which are evident as spikes in errors and uncertainty. On the fourth revolution are red arrows indicating the timespan in which vectors are saved for predictions and comparisons. The first and last red arrow point at perilune passages bounding the fourth NRHO revolution.

The results are an array of plots and statistics comparing the predictive state errors against the propagated filter covariance. This analysis is executed for predictions starting anywhere around the NRHO for up to one revolution. For this paper, predictions starting at $\nu = 150.0°$ and $\nu = 201.0°$ are given focus. HLS and LM depart for disposal at $\nu = 150.0°$ while VV arrivals occur near $\nu = 165°$, and OMMs are executed at $\nu = 200.0°$. Predictions are started at $\nu = 150.0°$ and $\nu = 201.0°$, then errors and covariance are sampled every three hours to create a series of snapshots of estimation error evolution through the predictions.

Figures 6, 7, 8, and 9 show prediction errors and filter covariance after predicting for zero, 63, 117, and 144 hours from $\nu = 150.0°$, respectively. Figure 6 shows estimation errors right at $\nu = 150.0°$ as points and filter covariance as ellipses. The plots are two dimensional planes centered on the truth state in the Earth Moon rotating frame. The filter covariance major axis is not aligned with the estimation errors, and the minor axis is larger than the error dispersion distribution.

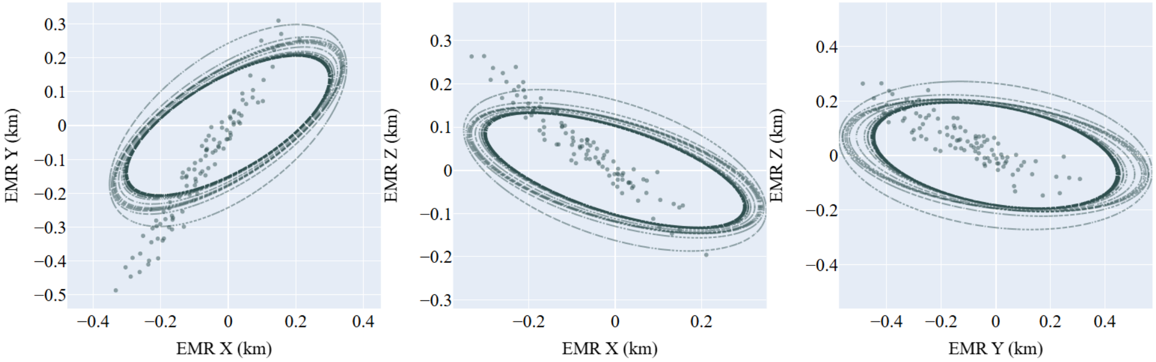

**Figure 6: Prediction errors (points) and filter covariances (ellipses) at $\nu = 150.0°$.**

Figure 7 shows estimation errors and filter covariance projected on Earth Moon rotating aligned planes after 63 hours of prediction, placing the estimated states at $\nu = 179.6°$, near apolune. Here, the estimation errors are well-defined by the filter covariance in the X-Y and Y-Z planes, but in the X-Z plane the minor axis of the covariance is larger than the distribution of estimation errors.

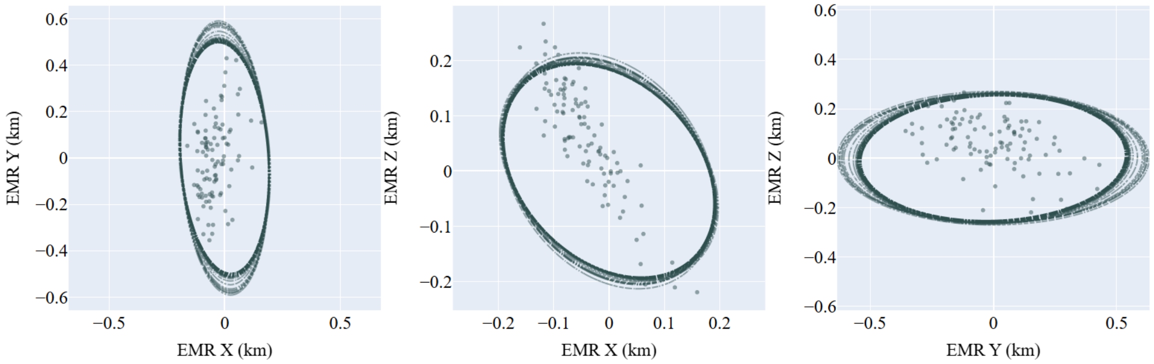

**Figure 7: Prediction errors (points) and filter covariances (ellipses) 63 hours after a prediction from $\nu = 150.0°$, now at $\nu = 179.6°$.**

Figure 8 shows estimation errors and filter covariance projected on Earth Moon rotating aligned planes after 63 hours of prediction, placing the estimated states at $\nu = 200.3°$, at the nominal location of the next OMM execution. At this point some secular bias between estimated states and truth are evident. The filter covariance bounds the errors but could be smaller if the secular bias were accounted for. As it is, the filter covariance is conservative and offset by a position bias.

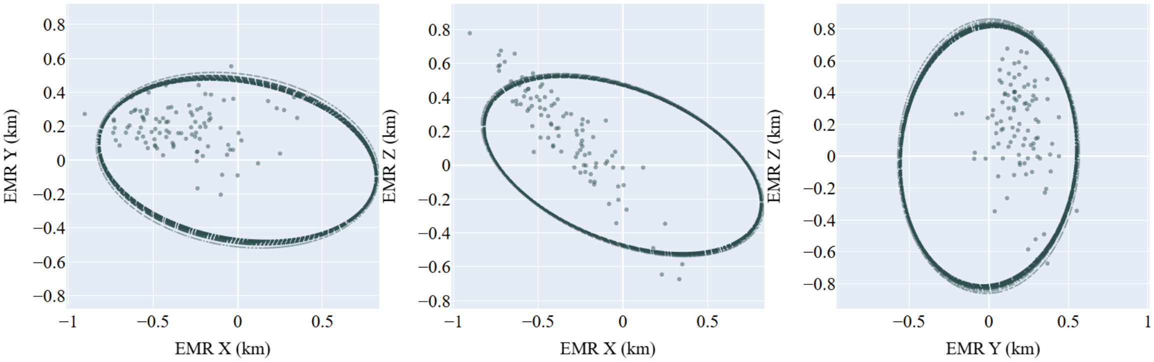

**Figure 8: Prediction errors (points) and filter covariances (ellipses) 117 hours after a prediction from $\nu = 150.0°$, now at $\nu = 200.3°$.**

Finally, Figure 9 shows estimation errors and filter covariance projected on Earth Moon rotating aligned planes after 144 hours of prediction, placing the estimated states at $\nu = 355.5°$, near perilune. Here the dynamics are coupled, leading to strong correlations. The major axis of the covariance is misaligned with the estimation error distribution, which are highly correlated.

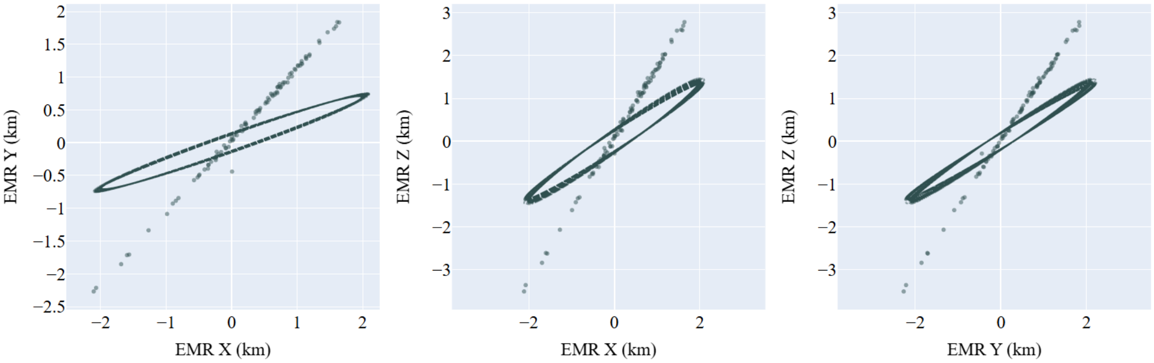

**Figure 9: Prediction errors (points) and filter covariances (ellipses) 144 hours after a prediction from $\nu = 150.0°$, now at $\nu = 355.5°$.**

OMMs are nominally executed centered at $\nu = 200.0°$, which make downstream predictions relatively important for operational calculations. Figure 10 shows estimation errors and filter covariances after OMM execution. Here there are several filter covariances larger and distinct from the consensus family of most of the Monte Carlo iterations. These covariances come from iterations where an OMM was executed on the fourth NRHO revolution, which triggers an instant step in velocity covariance diagonal magnitude equal to 1% of the OMM magnitude. These predictions begin before the subsequent post-OMM tracking data pass, which typically resolves the post-OMM velocity covariance delta. Additionally, there is a discernible bias to the errors in the X-Y and Y-Z plane, which if accounted for could allow for smaller covariance and thus more accurate stochastic calculations.

Figure 11 shows estimation errors and filter covariance projected on Earth Moon rotating aligned

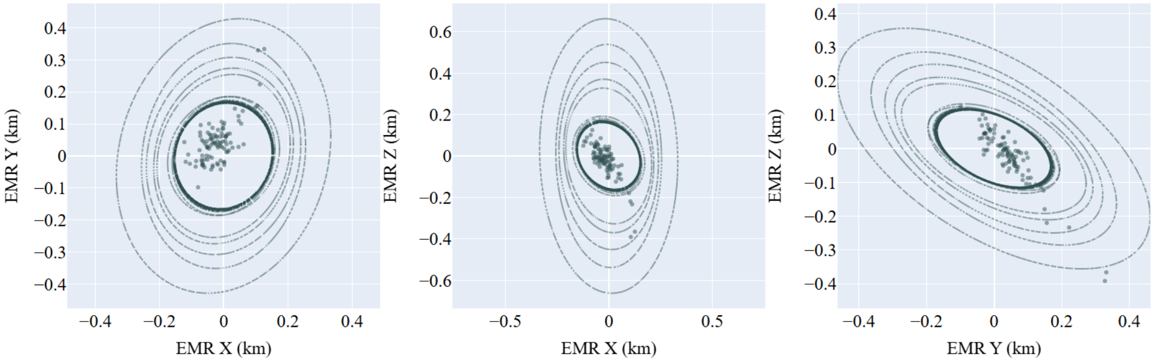

**Figure 10: Prediction errors (points) and filter covariances (ellipses) at $\nu = 201.0°$.**

planes after 21 hours of prediction, placing the estimated states at $\nu = 78.9°$. Though this is not at perilune, the dynamics here are still highly coupled. The covariance major axis is not aligned with the error distribution in the X-Y plane, and there are several outliers that escape filter covariance. Due to the highly dynamic geometry of the NRHO and the three-hour step size of extracting points for plots, this was the closest point to perilune from the solution set. In the X-Z and Y-Z planes the errors are misaligned with the covariance major axis but also are bounded by the covariance.

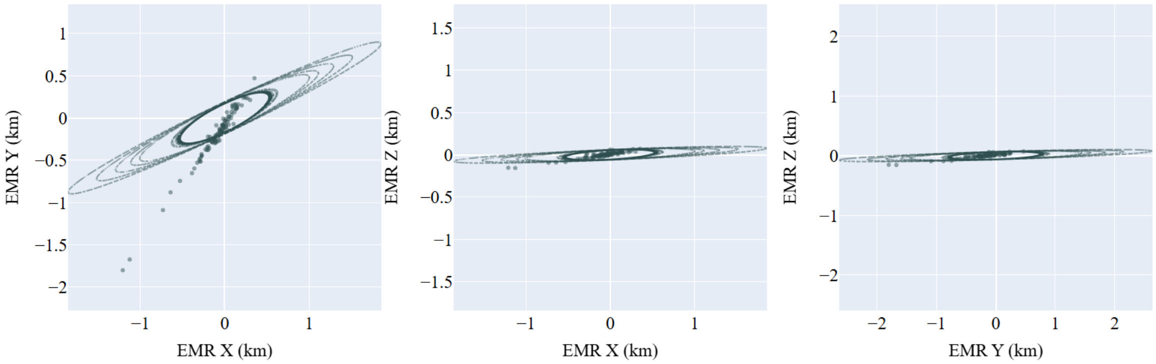

**Figure 11: Prediction errors (points) and filter covariances (ellipses) 21 hours after a prediction from $\nu = 201.0°$, now at $\nu = 78.9°$.**

Figure 12 shows estimation errors and filter covariance projected on Earth Moon rotating aligned planes after 21 hours of prediction, placing the estimated states at $\nu = 151.3°$. Predictions to $\nu = 150°$ are important to model errors and uncertainties at a potential location for VV arrival and docking. Here the errors are largely bounded by the covariance in all three EMR planes, but there is a bias which places most of each set of errors in a particular quadrant of their respective plot. A more accurate prediction which would center these errors at the origin would then allow for smaller and more precise filter covariances.

Figure 13 shows estimation errors and filter covariance projected on Earth Moon rotating aligned planes after 21 hours of prediction, placing the estimated states at $\nu = 180.4°$. Now near apolune, this is the point of lowest relative velocities and a point where OMMs can be executed if the nominal execution time interferes with mission activities. The errors are mostly bounded by the covariance, but the biased behavior continues. Removing the prediction bias could allow for smaller covariances.

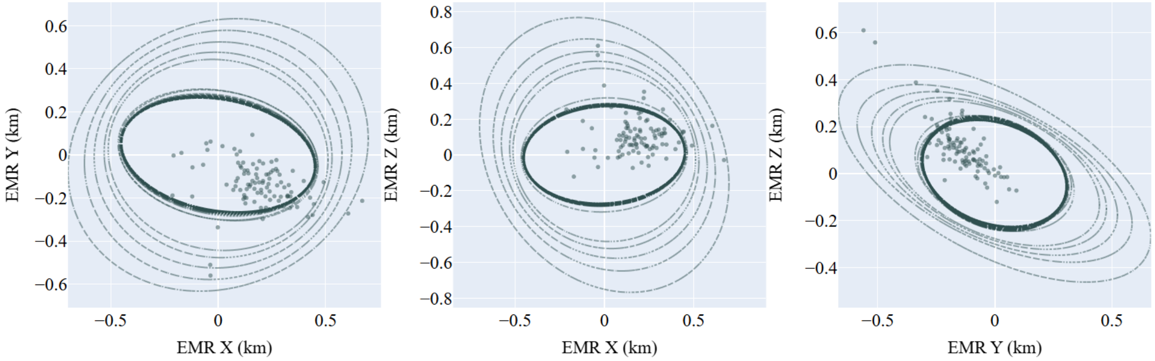

**Figure 12: Prediction errors (points) and filter covariances (ellipses) 42 hours after a prediction from $\nu = 201.0°$, now at $\nu = 151.3°$.**

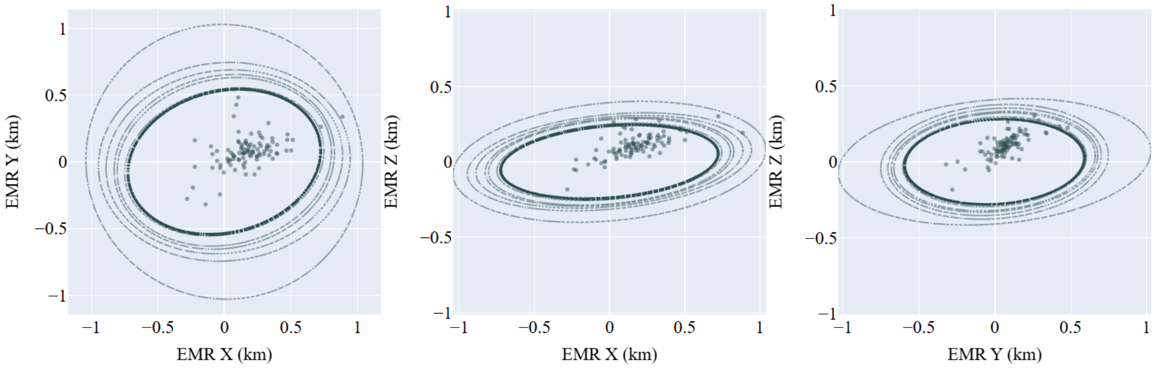

**Figure 13: Prediction errors (points) and filter covariances (ellipses) 108 hours after a prediction from $\nu = 201.0°$, now at $\nu = 180.4°$.**

## Discussion

Filter state estimates and covariances are propagated starting from various points around the NRHO and compared to the truth trajectory to determine the accuracy of predictions and the accuracy of the filter covariance to model estimation errors. For the paper, two starting positions are considered: at $\nu = 150.0°$ near where VV arrive and depart for disposal, and at $\nu = 200.0°$ where OMMs are nominally executed. In the cases analyzed for the paper there are two regimes of behavior: near perilune and away from perilune. Near perilune, the errors are highly correlated and the covariance is "squished" along its major axis. The errors are misaligned with the covariance, and due to the shape of the covariance in this regime, many errors exceed the bounds of the covariance. Away from perilune, the covariance is more spherical and estimation errors are more well bounded by it. There exists a persistent state estimation bias that tends to push estimation errors into a common quadrant of the EMR plane plots. More accurate predictions that would remove this bias could in turn allow for smaller covariance bounds and more accurate stochastic calculations which utilize those inputs.

Further work is necessary to determine the source of the error and covariance correlation misalignment near perilune, as well as the source of the estimation error bias away from perilune. More rigorous statistical comparisons of error distribution to filter covariance is warranted. Propagating filter covariances with unscented transforms may improve prediction accuracy and capture nonlinear dynamics. Additional errors could be introduced to initial estimation errors to "clone" predictions from a single state estimate that can expand the analysis to consider the impact of unknown errors and forces to prediction quality. Finally, this analysis should be expanded to be parameterized across all nine Sun-Earth orientations avaiable in this NRHO.

## PERTURBATION RECOVERY

Planning an event utilizes the latest available estimated vehicle state to calculate the action for the event. E.g. to plan an OMM, the estimated state at DCO is propagated forward in time and is the input for maneuver targeting. Thus there is always a timespan between the estimated state at DCO and the epoch of the planned event. An event planned after an existing RPOD event will be influenced by that perturbation. For the filter to "recover" from this perturbation, post-RPOD tracking data is processed to observe the vehicle state change. How much tracking data, and how long the prediction from DCO to the next event are of interest in this analysis.

Following each RPOD event, tracking data is simulated and processed for 24 hours. Within that span, state estimate vectors are saved for executing predictions. From each vector a prediction is generated, and vectors from that prediction are saved for comparison at times along each trajectory. The results are a Monte Carlo simulated set of predictions after RPOD events that consider varying amounts of post-RPOD tracking data. Ultimately, the vectors and predictions are meant to determine navigation performance downstream of an RPOD event, depending on the amount of post-RPOD tracking data processed and the time of flight of the subsequent prediction.

### HLS Mission Timeline

**Table 3: Event timeline for a notional HLS mission timeline**

| NRHO revolution | Event |
|---|---|
| 0-3 | Uncrewed operations |
| 4 | LM docks |
| 5 | HLS docks and undocks |
| **8** | HLS docks |
| **9** | Orion docks |
| **9** | HLS undocks for lunar sortie |
| **11** | HLS returns from lunar sortie |
| **11** | Orion undocks for Earth return |
| **12** | HLS undocks for departure |
| 13 | LM undocks for departure |

The state estimate recovery following a known perturbation is analyzed on a notional HLS mission timeline. Table 3 lists the NRHO revolution and configuration changes in this notional timeline. Configurations with a bold revolution number are tracked at the high cadence of three six hour passes per day. The simulation begins with four revolutions of uncrewed operations to achieve steady state behavior before mission events. The Logistics Module (LM) docks on the 4th revolution, and the HLS docks and undocks to loiter on revolution 5. After a three revolution duration loiter, HLS returns to dock on the eighth revolution. As the bold NRHO revolution number in Table 3 indicates, it is at this time that the filter begins processing high cadence (18 hours per day) tracking data. Orion docks with crew which transfer to HLS and depart for the lunar surface sortie on the 9th NRHO revolution. The HLS is away for a full revolution and returns on the 11th revolution. The crew transfers and departs on Orion on the same revolution. HLS then departs on the 12th revolution, which ends the high tracking data cadence. Finally, the LM departs on the 13th revolution.

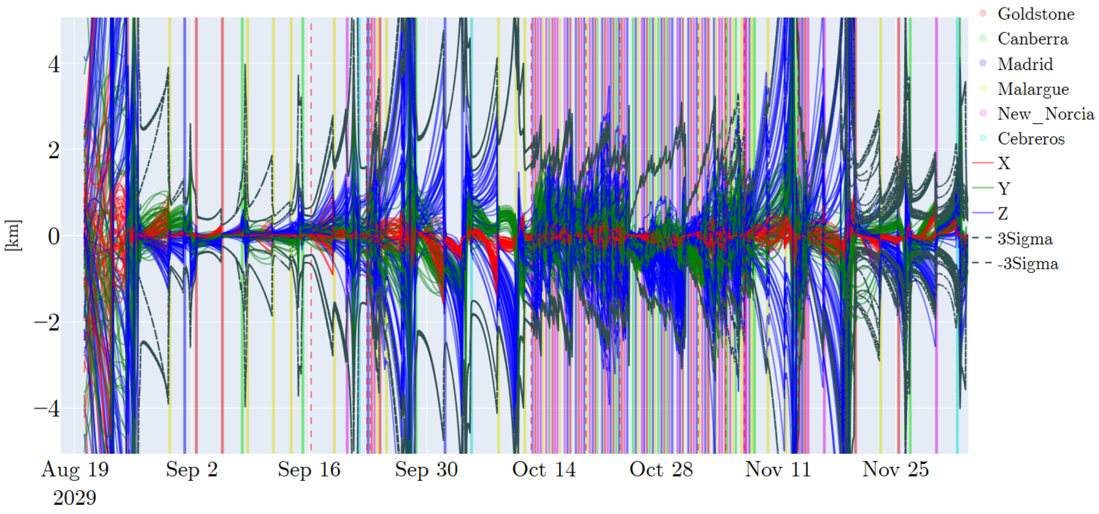

**Figure 14: Position errors and filter sigma over the HLS mission timeline. RPOD events are marked with vertical dashed red lines.**

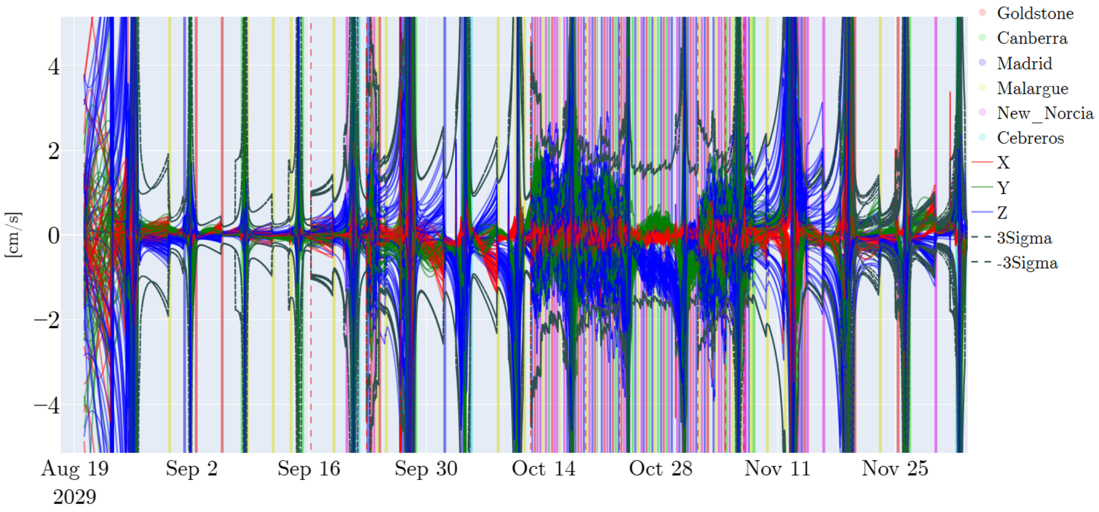

**Figure 15: Velocity errors and filter sigma over the HLS mission timeline. RPOD events are marked with vertical dashed red lines.**

The estimated position and velocity errors over the aforementioned HLS mission timeline are shown in Figures 14 and 15, respectively. There are four qualitative regions of navigation behavior in this simulation: First the simulation initializes and converges to steady state behavior. On the 5th revolution HLS docks and undocks to loiter, which causes an increase in errors. On the 8th revolution HLS returns to dock which begins the high cadence tracking (evident as the densely highlighted region of many tracking data passes). The HLS performs its lunar surface sortie, returns, then departs. The HLS departure is evident as another increase in errors that returns to steady state behavior after multiple uncrewed revolutions.

To evaluate the estimated state recovery following an RPOD event, tracking data is simulated post-RPOD and predictions are generated starting at various times post-RPOD. The first RPOD event scrutinized is the recovery following the HLS dock and undock for loiter on the fifth revolution. A detailed view of estimation errors and tracking data spans during the recovery period after the HLS RPODs are shown in Figure 16. The HLS dock and undock are represented as two vertical dashed red lines about ten hours apart. After the RPOD events, there are multiple tracking data passes to reduce the errors and uncertainties. Focusing on the velocity errors in Figure 16b, note how handovers to a different ground site cause a reduction in filter uncertainty. This is most prominent in the handover from Madrid to Goldstone before 12:00 on September 24. Figure 17

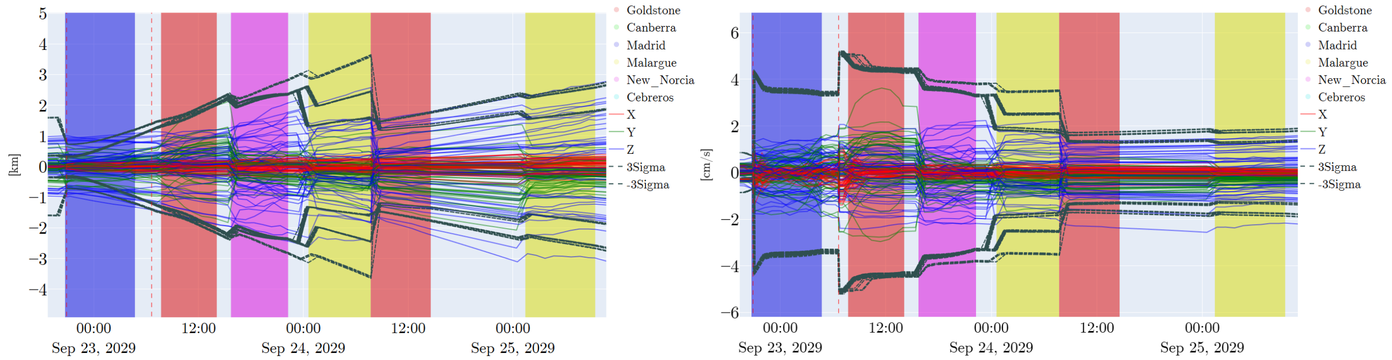

(a) Position

(b) Velocity

**Figure 16: Navigation errors in the temporal proximity of HLS dock and undock on the fifth revolution.**

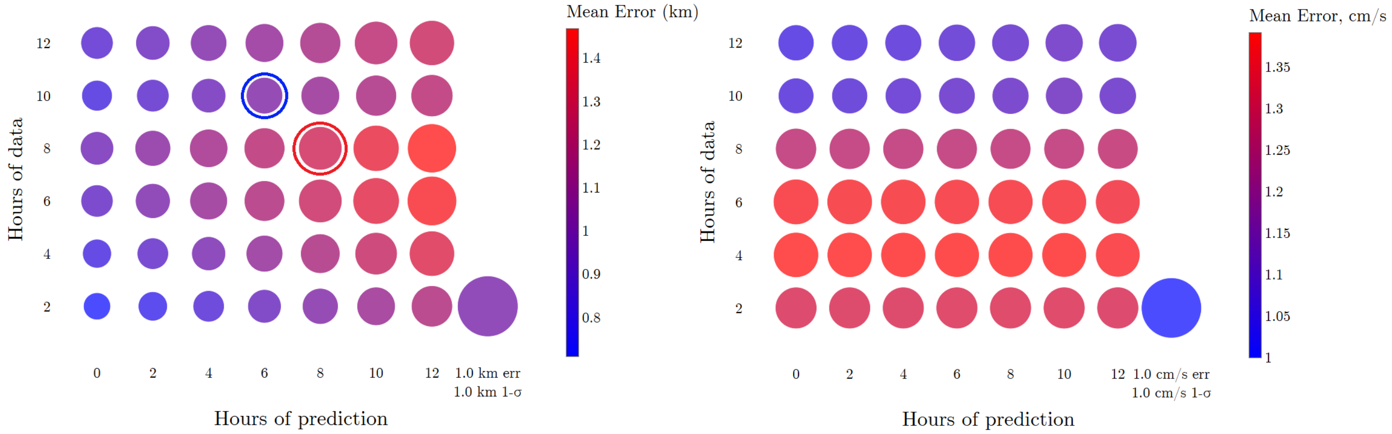

(a) Position

(b) Velocity

**Figure 17: Recovery Matrices for post-HLS undock for loiter on fifth revolution.**

shows what is heretofore referred to as the *Recovery Matrices* of this RPOD event pair. The recovery matrix is a bubble chart that links post-RPOD tracking data, post-DCO prediction timespan, and estimation performance. Each circle's color and radius correspond to the average error and 1-$\sigma$ dispersion, respectively. A small blue circle represents low error and sigma, while a large red circle indicates high error and sigma. A color bar on the right links color to mean error, and a "unity bubble" plotted bottom right links radius to sigma.

The chart can be read by choosing timespans for tracking data and post-DCO prediction and finding the corresponding bubble to see its performance relative to other combinations. E.g. in Figure 17a, processing eight hours of tracking data and predicting eight hours will return position estimation performance indicated by the bubble circled in red. If however tracking data is processed for ten hours and then that DCO vector predicted for six hours, the performance will be that indicated by the bubble circled in blue. Both combinations add to sixteen hours between events, but the extra two hours of tracking data will include the aforementioned handover to Goldstone which reduces errors and dispersions. The influence of this handover is more evident in velocity in Figure 17b, where the top two rows of bubbles have lower mean error and variance. Processing ten hours of data post-RPOD improves estimation performance for any subsequent prediction downstream.

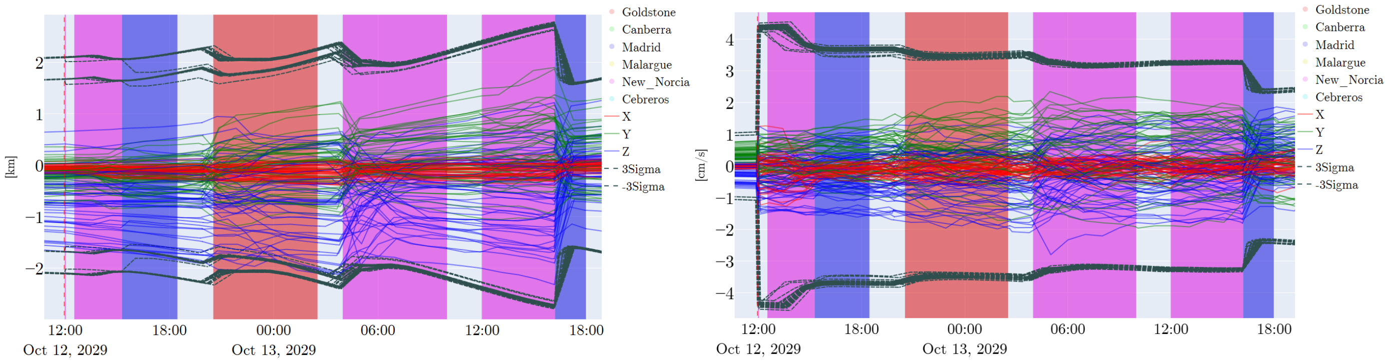

(a) Position

(b) Velocity

**Figure 18: Navigation errors after HLS docking on the eighth revolution.**

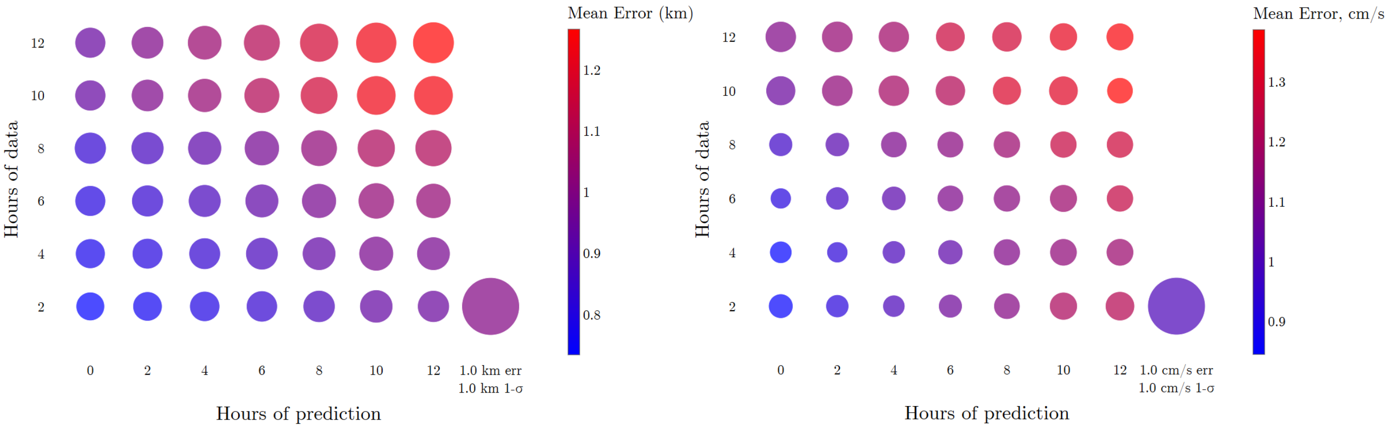

(a) Position

(b) Velocity

**Figure 19: Recovery Matrices for post-HLS docking on eighth revolution.**

Figure 18 shows the estimation errors and tracking data passes after HLS redocks on the eighth revolution. In position (Figure 18a), the errors from downstream tracking data passes and handovers between ground sites do not reduce the error or covariance. Likewise in velocity (Figure 18b), the covariance slightly reduces between ground site handovers, but the error distribution spreads out due to random perturbations from HLS. Note the Earth-Moon rotating X direction errors (in red) are lowest due to the X-direction being most co-aligned with the range direction from Earth ground sites. Those errors are exhibiting steady state behavior and are not reducing further from ground site tracking data processing.

The resulting recovery matrices for this RPOD event are shown in Figure 19. These results show monotonically increasing error mean and variances in both tracking data quantity and post-DCO prediction timespan. Figure 18 shows tracking data spans handover between New Norcia and Madrid or Goldstone. Handovers show a slight reduction in velocity uncertainty, but the perturbations in the Y and Z diretion grow due to unobservability. Adjusting the tracking schedule to increase handovers and reduce reliance on New Norcia could slightly improve performance, but the perturbations normal to the range direction will remain unobservable. There is not a downstream handover that improves the estimation performance which could guide operations to request such data—errors steadily increase regardless downstream of this RPOD event.

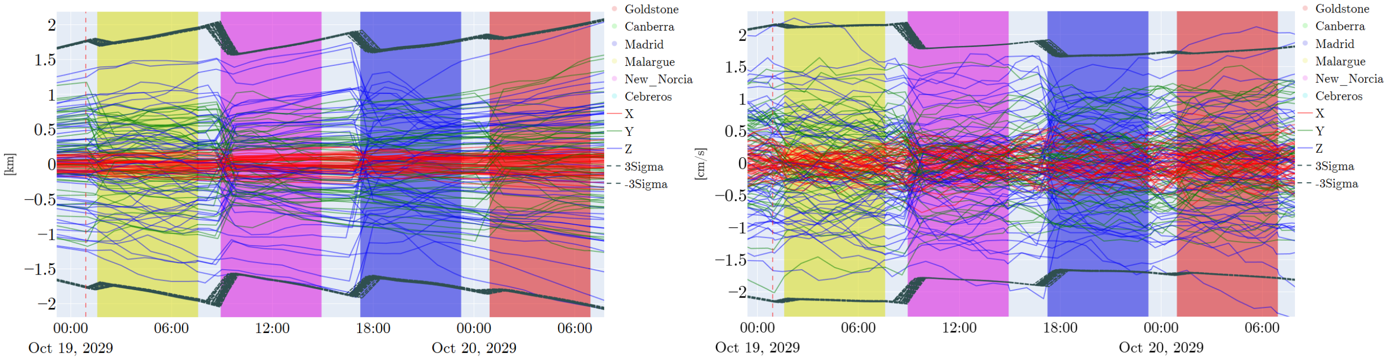

(a) Position (b) Velocity

**Figure 20: Navigation errors after Orion docks on the ninth revolution.**

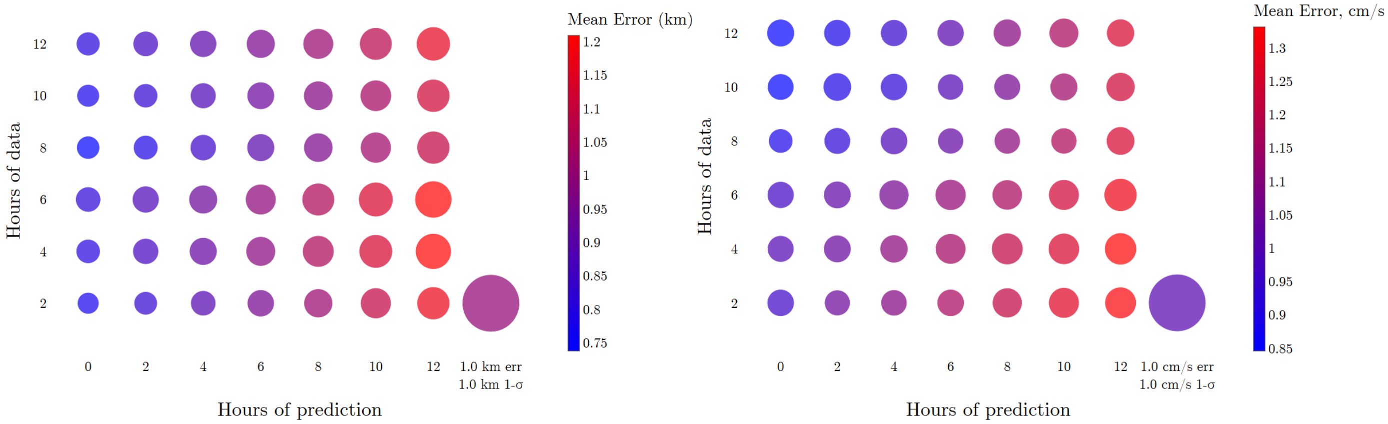

(a) Position (b) Velocity

**Figure 21: Recovery Matrices for post-Orion dock on the ninth revolution..**

Figure 20 shows the estimation errors and tracking data passes after Orion docks on the ninth revolution. There are two handovers that reduce the position and velocity uncertainty which influence the recovery behavior. Figure 21a shows the benefit of post-RPOD tracking data—position errors seem to minimize after eight hours of tracking data, above which errors begin to rise again. Introducing more ground site handovers could further reduce uncertainty, especially between ground sites across the Earth equator. Introducing more data types such as three-way doppler could also improve the observation geometry and reduce estimation uncertainty.

Figure 22 shows the estimation errors and tracking data passes after HLS undocks for the lunar

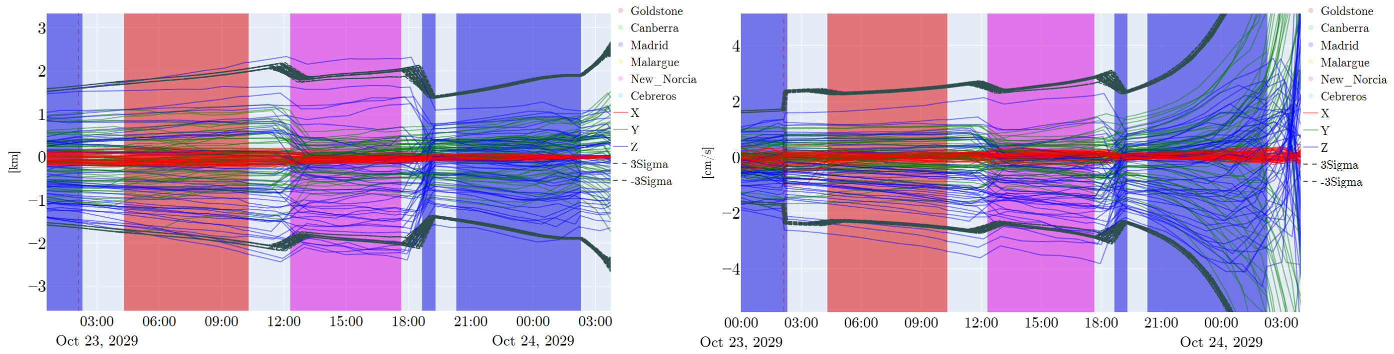

(a) Position

(b) Velocity

**Figure 22: Navigation errors after HLS undocks for the lunar surface sortie on the ninth revolution.**

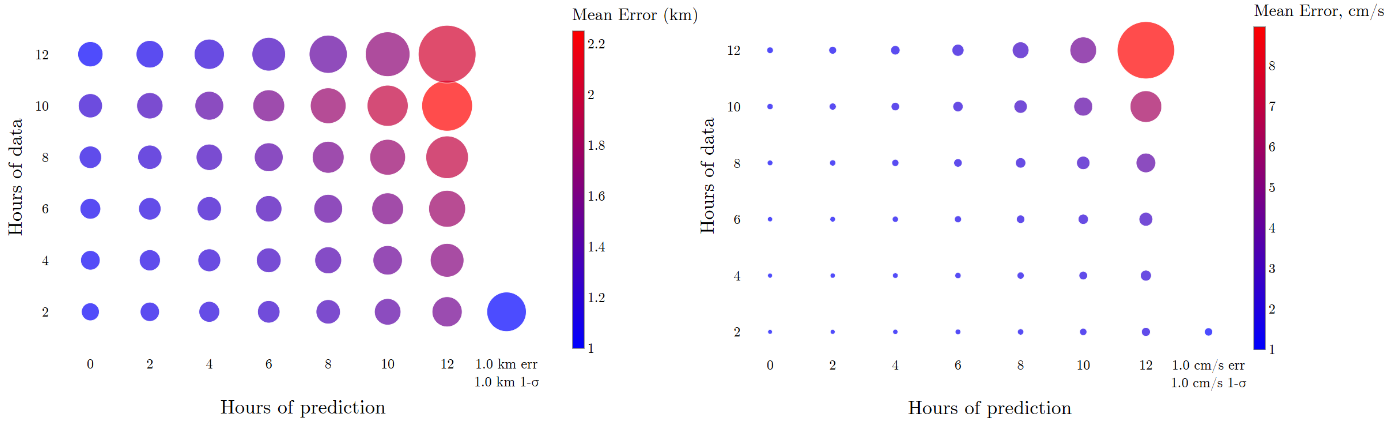

(a) Position

(b) Velocity

**Figure 23: Recovery Matrices for post-HLS undock for the lunar surface sortie on the ninth revolution.**

surface sortie on the ninth revolution. The HLS undocks for the lunar surface sortie at $\nu = 200.3^\circ$, roughly one day before perilune passage. This is evident in the spike in velocity errors shown in Figure 22b. The recovery matrices for this RPOD event are shown in Figure 23. Perilune passage drives the growth in error for predictions starting downstream of the RPOD event. The estimation error spike from perilune passage is relatively brief in time. Looking at Figure 23b, the velocity errors grow quickly only after 20 hours after the RPOD event.

Figure 24 shows the estimation errors and tracking data passes after HLS returns from the lunar surface sortie on the 11th revolution. After this RPOD event, every ground site handover results in a consistent reduction in filter uncertainty and a slight improvement in errors (which quickly unravel as velocity perturbations dominate). The corresponding recovery matrices are shown in Figure 19. Errors after post-RPOD DCO increase monotonically until after eight hours of tracking data. A handover between then and 10 hours causes a reduction in position and velocity estimation errors.

Figure 26 shows the estimation errors and tracking data passes after Orion departs for Earth return on the 11th revolution. In the period of time following this RPOD event, there is a reduction in errors and uncertainty at the first ground site handover to Canberra, but subsequent handovers do not affect errors or covariance appreciably. Figure 27 shows the recovery matrices for this RPOD

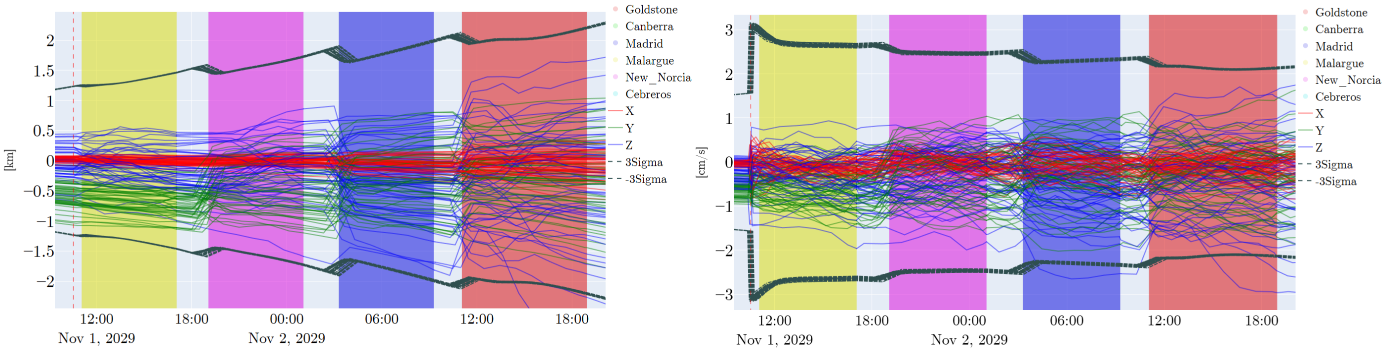

(a) Position (b) Velocity

**Figure 24: Navigation errors for post-HLS return from the lunar surface sortie on the 11th revolution.**

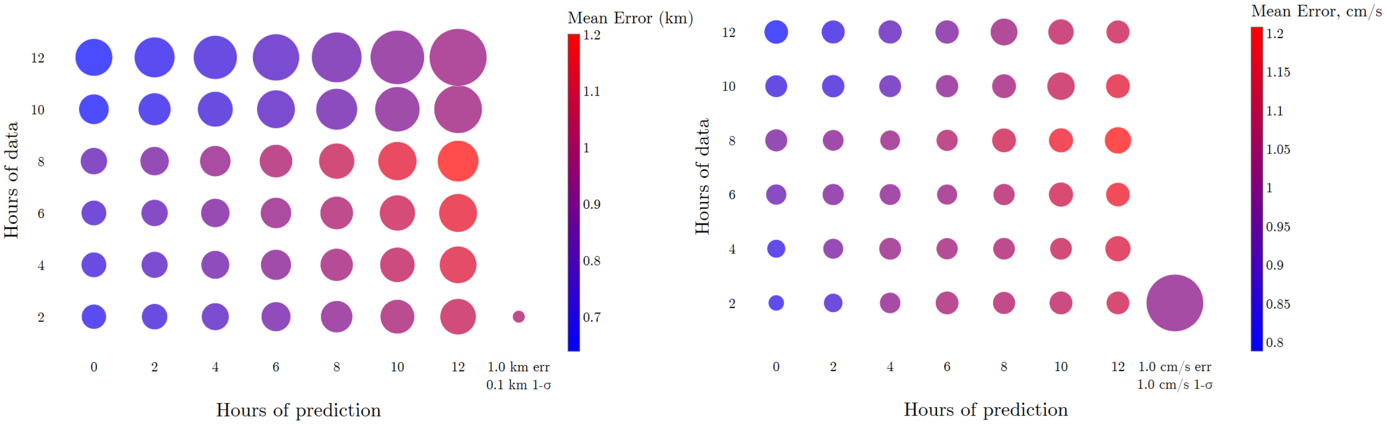

(a) Position (b) Velocity

**Figure 25: Recovery Matrices for post-HLS return from the lunar surface sortie on the 11th revolution.**

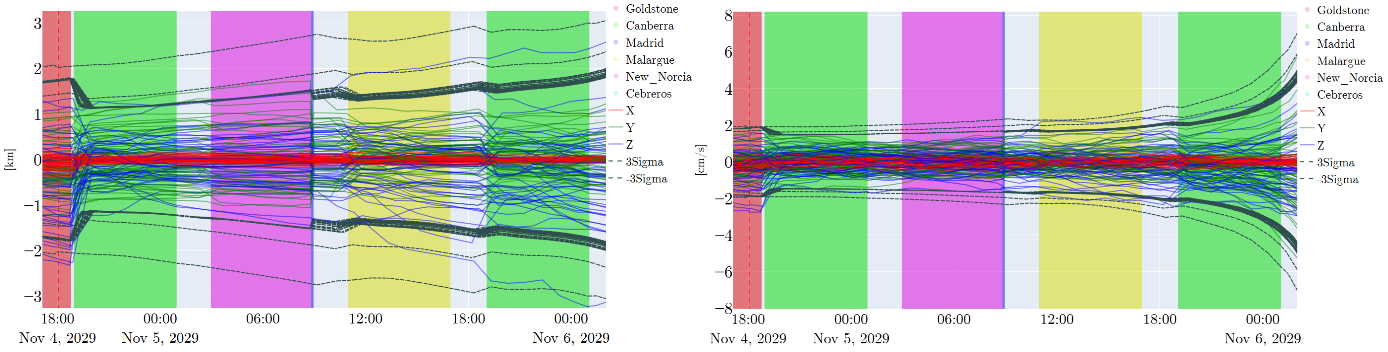

(a) Position (b) Velocity

**Figure 26: Navigation errors for post-Orion departure on the 11th revolution.**

event, and there does not seem to be a singular timespan of tracking data that causes a significant reduction in uncertainties. There is a slight reduction in velocity error sigma between zero and four hours regardless of processing tracking data or not evident in Figure 27b. Excepting that, estimation errors grow monotonically for increasing timespans between this RPOD and a future event.

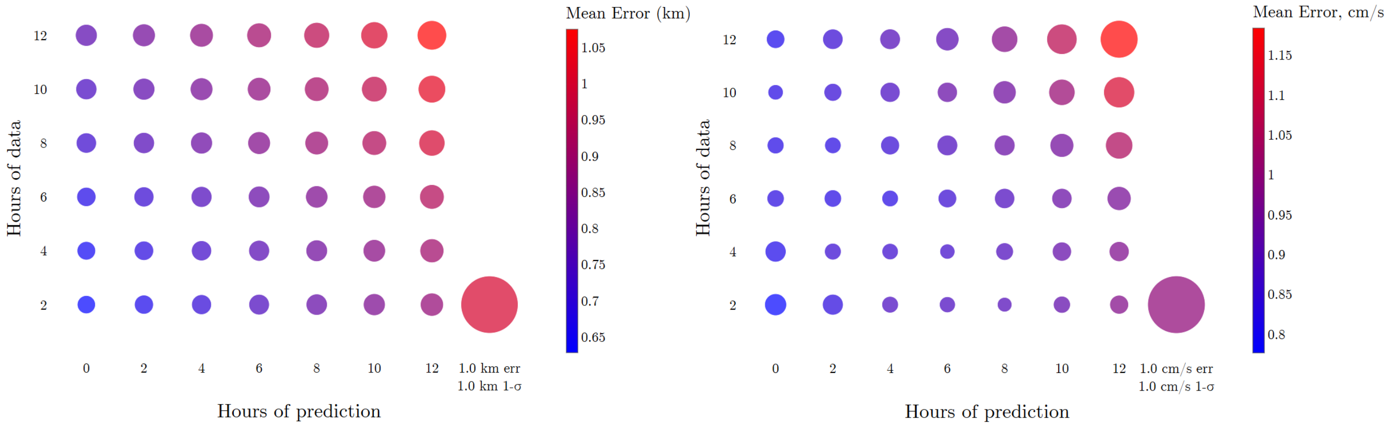

(a) Position (b) Velocity

**Figure 27: Recovery Matrices for post-Orion departure on the 11th revolution.**

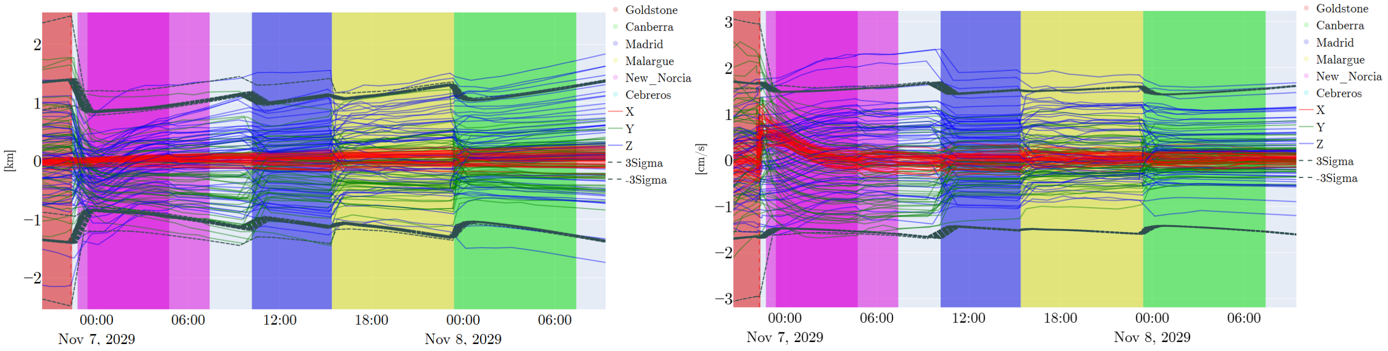

(a) Position (b) Velocity

**Figure 28: Navigation errors for post-HLS disposal on the 12th revolution.**

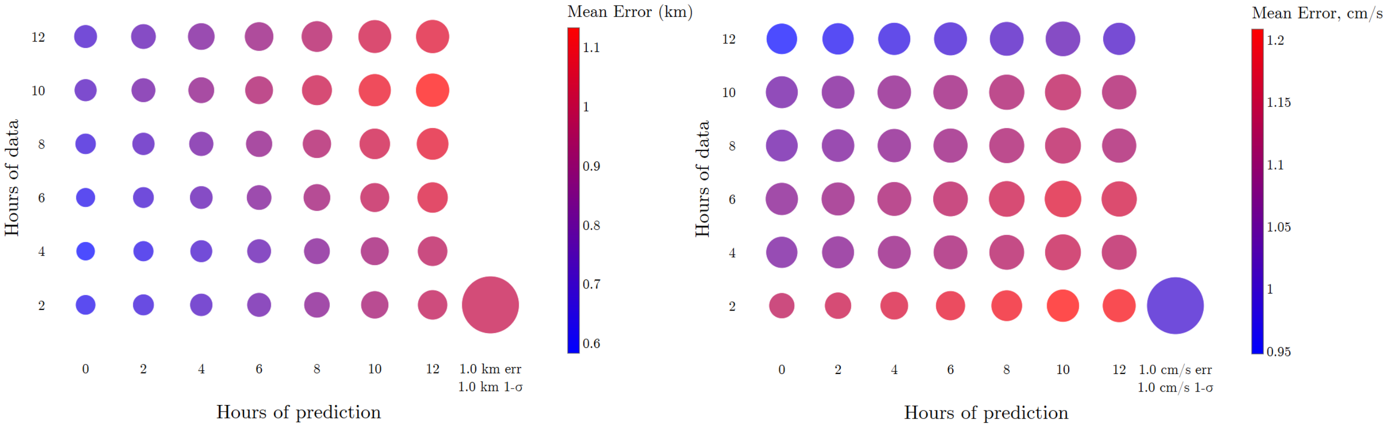

(a) Position (b) Velocity

**Figure 29: Recovery Matrices for post-HLS disposal on the 12th revolution.**

Figure 28 shows the estimation errors and tracking data passes after HLS departs for disposal on the 12th revolution. There is a distinct reduction in position uncertainty at the start of the first post-RPOD tracking data pass (Figure 28a), but subsequent ground site handovers do not exhibit strong reductions in errors and uncertainty. There is a reduction in velocity uncertainty at the start of the Madrid tracking data pass (Figure 28b) roughly ten hours after the RPOD event. Likewise, velocity errors shown in Figure 29b are reduced in the row of predictions after 12 hours of tracking data processing. There is also a reduction in average error (but a rise in error distribution sigma) between two and four hours of tracking data processing.

## CONCLUSIONS AND FORWARD WORK

Covariance propagation in the NRHO is validated using Monte Carlo simulation methods. Due to the dynamic geometry of the NRHO, covariance propagation validation is location and time of flight dependent. State estimate predictions are started at various points around the NRHO and propagated for one revolution. State estimate errors and covariance are sampled along the prediction and plotted on Earth Moon rotating planes for comparison.

It was found that there is generally two modes of covariance behavior: a stretched, highly correlated covariance near perilune, and a more spherical covariance away from perilune. Near perilune, the sampled estimation errors do not align with the covariance, which with the highly correlated shape of the covariance results in many state estimate errors outside the covariance. Away from perilune estimation errors are bounded by the associated covariance, but are not zero-mean within the covariance. A secular estimation bias persists which reduces the accuracy of the propagated covariance. Removing the estimation bias could allow for a tighter covariance that more accurately captures the distribution of estimation errors.

Future work in covariance validation includes adjusting force modeling and covariance propagation methods to improve accuracy. Nonlinear covariance propagation methods such as unscented or sigma point propagation may improve performance. The analysis considers predictions of varying time length from various points along the NRHO but should expand to parameterize across the nine Earth-Sun oriented NRHO orientations. It is likely that the perilune error correlation and secular bias away from perilune are both solar orientation dependent. Finally, refinements to the visualization of the errors and covariance statistics will help interpret the results for the context of NRHO operations.

Estimation error recovery following RPOD events is investigated using Monte Carlo simulation methods. Estimation error recovery is dependent on post-RPOD tracking data processing and prediction time length post-DCO (of the post-RPOD tracking data). Considering a notional HLS mission event timeline, post-RPOD tracking data is processed and multiple post-RPOD DCO states are saved. Predictions from each post-RPOD DCO state estimate are generated. The post-RPOD estimation errors as a function of post-RPOD tracking data quantity and post-DCO prediction time length are organized as bubble plots in this paper to quickly relay the post-RPOD recovery behavior based on those inputs.

For many RPOD events (namely the HLS undock on the fifth revolution, Orion dock on the ninth, and the HLS return from the lunar sortie on the 11th), there is a post-RPOD handover between scheduled ground sites that significantly improves estimation error and uncertainty. Estimation errors will increase regardless of processed tracking data until that handover, which will see errors thereafter reduced. These are evident as a reduction in error across a horizontal row of bubbles at a particular time, e.g. after eight hours of tracking in Figure 17b. For other RPOD events (namely HLS docking on the eighth revolution and Orion departure on the 11th) estimation errors grow monotonically regardless of amount of tracking data processed. For these situations, the tracking data schedule did not allow for handovers that result in a reduction of state estimate uncertainty. Finally, the time span following HLS undock for the lunar surface sortie includes a perilune passage, which drives error growth behavior of recovery predictions.

Future work in RPOD recovery analysis will investigate methods to improve recovery performance and broaden the analysis to include more solar orientations and mission timelines. The limited geometry of range observations makes recovery difficult in all three axes, and drives the influence of ground site handovers to reducing filter uncertainty. Adjusting the ground site selection algorithm to maximize observation geometry could improve recovery performance. Inclusion of additional data sources such as relative inter-vehicle ranging or three-way doppler can also improve observation geometry.

## ACKNOWLEDGEMENTS

The authors would like to thank Aurelie Heritier, Anthony Zara, and Connor Plaks from Advanced Space, Inc. for their technical collaboration on this project. This work was completed through contract # NNJ13HA01C.

## REFERENCES

[1] R. Whitley and R. Martinez, “Options for Staging Orbits in Cis-Lunar Space,” *2016 IEEE Aerospace Conference*, 2016.

[2] D. E. Lee, “White Paper: Gateway Destination Orbit Model: A Continuous 15 Year NRHO Reference Trajectory,” Tech. Rep. Document ID: 20190030294, National Aeronautics and Space Administration, NASA Johnson Space Center, Houston, TX, August 2019.

[3] D. C. Davis, F. S. Khoury, and K. C. Howell, “Phase Control and Eclipse Avoidance in Near Rectilinear Halo Orbits,” *AAS Guidance, Navigation, and Control Conference*, Breckenridge, Colorado, February 2020.

[4] D. C. Davis, F. S. Khoury, K. C. Howell, and D. J. Sweeney, “Phase Control and Eclipse Avoidance in Near Rectilinear Halo Orbits,” *Paper No. AAS 20-047, AAS Guidance, Navigation, and Control Conference, Breckenridge, Colorado*, January 2020.

[5] D. Guzetti, E. M. Zimovan, K. C. Howell, and D. C. Davis, “Stationkeeping Analysis for Spacecraft in Lunar Near Rectilinear Halo Orbits,” *Paper No. AAS-2017-395, AAS/AIAA Spaceflight Mechanics Meeting, San Antonio, Texas*, February 2017.

[6] B. McCarthy, S. Schuerle, E. Zimovan-Spreen, and D. Davis, “Strategies and Applications for Sustained Multi-Vehicle Loitering in the Gateway NRHO,” *2025 AAS/AIAA Space Flight Mechanics Meeting*, Kaua’i, HI, January 2025.

[7] J. Silva-Martinez, “Development of Space Mission Integrated Operations Scenarios,” *17th International Conference on Space Operations*, Dubai, UAE, March 2023.

[8] C. P. Newman, D. C. Davis, R. J. Whitley, J. R. Guinn, and M. S. Ryne, “Stationkeeping, Orbit Determination, and Attitude Control for Spacecraft in Near Rectilinear Halo Orbits,” *Paper No. AAS 18-388, AAS Astrodynamics Specialist Conference, Snowbird, Utah*, August 2018.

[9] E. S. A. (ESA), “Estrack: ESA’s global ground station network,” `https://www.esa.int/Enabling_Support/Operations/ESA_Ground_Stations/Estrack_ESA_s_global_ground_station_network`.

[10] C. Ott, M. Bollinger, M. Thompson, and N. P. Re, “Range Biases, Measurement Noise, and Perilune Accuracy in Near Rectilinear Halo Orbit Navigation,” *AIAA Scitech Forum and Exposition*, San Diego, California, January 2022.

[11] N. Parrish, M. J. Bollinger, E. W. Kayser, M. R. Thompson, J. S. Parker, B. W. Cheetham, D. C. Davis, and D. J. Sweeney, “Near Rectilinear Halo Orbit Determination with Simulated DSN Observations.,” *AIAA Scitech 2020 Forum*, Orlando, Florida, March 2020.

[12] D. C. Davis, S. A. Bhatt, K. C. Howell, J. Jang, R. L. Whitley, F. D. Clark, D. Guzzetti, E. M. Zimovan, and G. H. Barton, “Orbit Maintenance and Navigation of Human Spacecraft at Cislunar Near Rectilinear Halo Orbits,” *27th AAS/AIAA Space Flight Mechanics Meeting*, San Antonio, Texas, February 2017.

[13] C. P. Newman, J. R. Hollister, F. S. Miguel, D. C. Davis, and D. J. Sweeney, “Attitude Control and Perturbation Analysis of a Crewed Spacecraft with a Lunar Lander in Near Rectilinear Halo Orbits,” *AAS Guidance, Navigation, and Control Conference*, Breckenridge, Colorado, February 2020.

[14] J. R. Carpenter and C. D'Souza, *Navigation Filter Best Practices*. NASA Engineering and Safety Center, 2nd ed.